

Future Dynamics of the Local Group. I. MW-M31 Interactions

COLIN LEACH 

ABSTRACT

TODO Add a concise and intelligent summary of the paper, once I get a clearer idea what it will include (and how to seem intelligent).

Meanwhile, here is some nonsense:

Lorem ipsum dolor sit amet, consectetur adipiscing elit. Ut purus elit, vestibulum ut, placerat ac, adipiscing vitae, felis. Curabitur dictum gravida mauris. Nam arcu libero, nonummy eget, consectetur id, vulputate a, magna. Donec vehicula augue eu neque. Pellentesque habitant morbi tristique senectus et netus et malesuada fames ac turpis egestas. Mauris ut leo. Cras viverra metus rhoncus sem. Nulla et lectus vestibulum urna fringilla ultrices. Phasellus eu tellus sit amet tortor gravida placerat. Integer sapien est, iaculis in, pretium quis, viverra ac, nunc. Praesent eget sem vel leo ultrices bibendum. Aenean faucibus. Morbi dolor nulla, malesuada eu, pulvinar at, mollis ac, nulla. Curabitur auctor semper nulla. Donec varius orci eget risus. Duis nibh mi, congue eu, accumsan eleifend, sagittis quis, diam. Duis eget orci sit amet orci dignissim rutrum.

Keywords: Galaxy Merger – Local Group – Stellar Disk – Stellar Bulge – Dark Matter Halo – Hernquist Profile – Merger Remnant

1. INTRODUCTION

The currently-accepted model of galaxy formation involves baryonic matter (gas and dust) falling into gravitational potential wells created by local over-densities in the Dark Matter (DM). Further gravitational collapse and Jeans fragmentation can then lead to creation of galaxies and stars (Mo et al. 2010).

However, decades of observational and theoretical studies tell us that, firstly, this by itself does not account for the wide range of galaxy morphologies seen at all epochs; secondly, there is no reason to suppose that galaxies continue in serene isolation after their formation.

Attempts to model interactions and mergers between galaxies with numerical simulations goes back at least to Toomre & Toomre (1972). This field continues to develop, with improvements in both hardware and algorithms allowing larger particle numbers in N-body simulations and more sophisticated treatment of gas hydrodynamics, magnetic fields and other factors (Bodenheimer et al. 2007).

As with all theoretical studies, it is vital to stay connected to the best experimental data as this constantly evolves, constantly comparing models against observations. Checking simulations against high-redshift galaxies is necessary but inevitably approximate. A perhaps

more rigorous test is to model the galaxies for which we have the most precise and detailed observational measurements: those which are (by far) closest to us.

The largest galaxies in our Local Group (LG) are the Milky Way (MW), Andromeda (M31) and Triangulum (M33). A simulation of MW–M31–M33 orbital evolution was described previously in Marel et al. (2012a), hereafter vdM12. That paper included an extensive analysis of both N-body simulations and semi-analytic orbit integrations. The present study uses data from the same N-body simulation to carry out further computational analysis.

The simulation was based on data in Marel et al. (2012b) suggesting that M31 is approaching the MW directly with little proper motion detected by Hubble Space Telescope studies. Recent data from Gaia DR2 (Brown et al. 2018) suggest that infall is slightly less radial than previously thought (Marel et al. 2019), leading to a slightly later first approach with a larger pericenter distance. However, detailed simulations based on that new data have not yet been carried out.

This paper will review the initial conditions and time evolution for multiple physical parameters of the simulation. Particular attention will be paid to the first MW-M31 close approach around 4 Gyr, the second ap-

proach and merger around 6 Gyr, and the structure and dynamics of the post-merger remnant.

Time probably precludes much analysis of the fate of M33, which will need to be the subject of a future paper.

1.1. Data

Data from one N-body simulation in vdM12 was supplied in text-file format by one of the original authors. This included position and velocity data for each particle at the current epoch ($t = 0$) and 800 future time steps. For ease of analysis, this was all transferred to the open source database PostgreSQL¹ (approximately 1.35 billion records). The same database was used to store computed summary data during the analysis.

Table 1. Particle counts

Galaxy	DM Halo	Disk	Bulge	Total
MW	250,000	375,000	50,000	675,000
M31	250,000	600,000	95,000	945,000
M33	25,000	46,500	0	71,500
LG	525,000	1,021,500	145,000	1,691,500

Particle counts for each time point are shown in Table 1 and total masses in Table 2. We can see that total mass is the same for MW/M31 but our galaxy has more dark matter (lower baryon fraction) and M31 has more luminous stars (higher baryon fraction). M33 is about 10-fold lighter than either.

Table 2. Aggregate masses ($M_{\odot} \times 10^{12}$)

Galaxy	DM Halo	Disk	Bulge	Total
MW	1.975	0.075	0.010	2.060
M31	1.921	0.120	0.019	2.060
M33	0.187	0.009	0.000	0.196
LG	4.082	0.204	0.029	4.316

The coordinate system is approximately centered on the Milky Way at $t = 0$. The center of mass (CoM) of all particles in the system is not fixed over time, moving at an average of $\vec{v} = \langle 35.9, -26.7, 27.5 \rangle$ km/s with some minor fluctuations due to numerical approximations. In

contrast, the total angular momentum of the system is very small at all time points.

1.2. Software

The work in this report was carried out in Python using standard packages. Full details are available online²

2. RESULTS

2.1. Trajectories

The simulation does not explicitly include a supermassive black hole (SMBH) at the center of each galaxy, but the galactic center was defined by calculating the center of mass (CoM) of the disk particles and iteratively constraining the radius of interest until convergence.

To plot motions of the three galactic CoMs it is convenient to transform to a coordinate system in which at $t = 0$ they all lie in the x, y plane with MW and M31 on the x -axis. The overall CoM is moving, as noted above, so at each time point the coordinates are translated to center it at the origin.

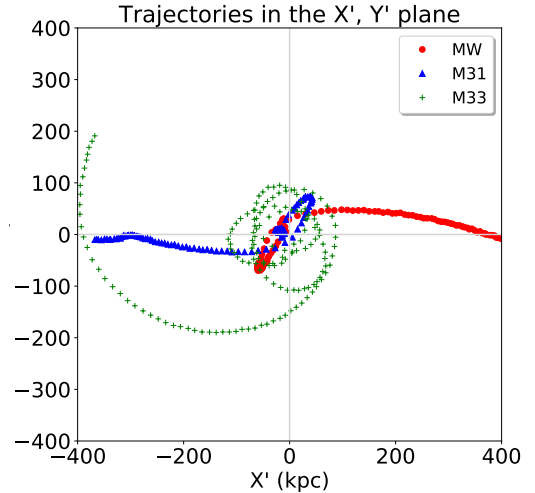


Figure 1. Trajectories of each galactic center of mass in the X', Y' plane. Points are at 71 Myr intervals.

In vdM12 this is referred to as the X', Y', Z' coordinate system and their figure 2 shows multiple views of how the galaxies move through time. In this paper, Figures 1 and 2 show some alternative views in essentially the same coordinates (up to a sign; the x and z axes are flipped). Figure 1 reproduces the top left panel of vdM12. Figure 2 shows that MW and M31 remain close

¹ <http://www.postgresql.org>

² Code https://github.com/colinleach/400B_Leach
documentation <https://400b-leach.readthedocs.io>

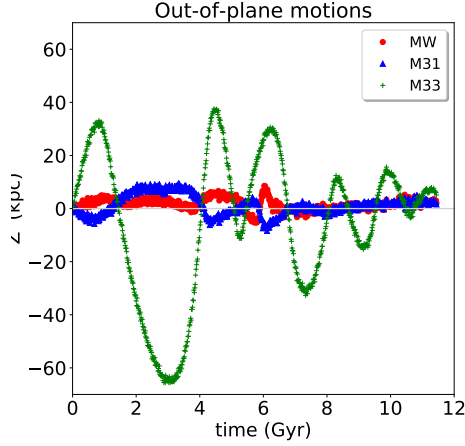


Figure 2. Trajectories of each galactic center of mass perpendicular to the X', Y' plane.

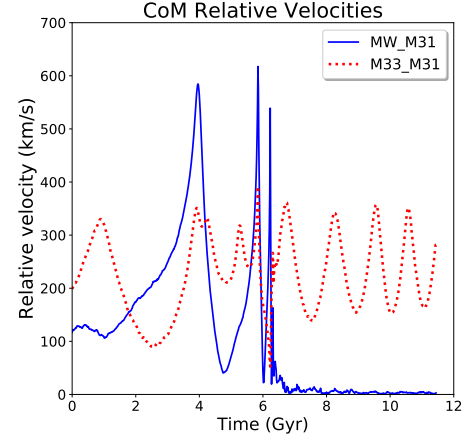


Figure 4. Relative velocities of galactic CoMs.

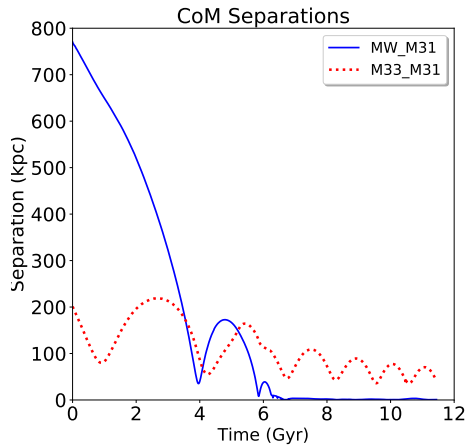


Figure 3. Separations of galactic CoMs.

to the starting plane while M33 has larger, irregular out-of-plane motions.

Relative motions of the CoMs are shown against time in Figures 3 and 4, equivalent to figures 3 and 4 in vdM12.

There is a MW-M31 close approach with first pericenter at 3.96 Gyr with a minimum separation of 35.1 kpc, then a separation to 173 kpc at apocenter and finally a convergence to 7.8 kpc at second pericenter and merger between 5.9 - 6.5 Gyr. Relative velocities spike sharply during these approaches, as potential energy is converted to kinetic energy, before declining to essentially zero.

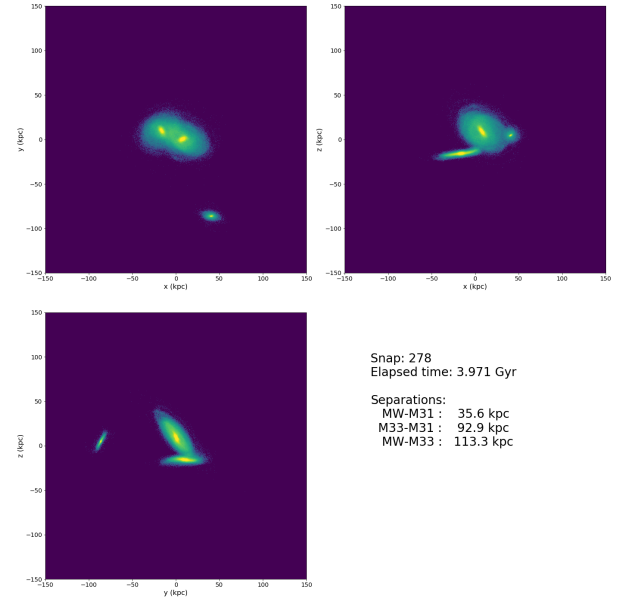


Figure 5. Orthogonal views of the three galaxies (disk particles only) at first apocenter. **TODO** improve this visually!

Figure 5 shows a view of first apocenter as a disk density plot from three orthogonal directions. The full animation is available online³

Meanwhile, in this simulation run M33 remains separate throughout, albeit on a decaying orbit. In vdM12 the authors investigate the effect of small changes in initial conditions and estimate a 9% chance of an M33-MW collision at first pericenter, before the M31-MW merger.

³ https://github.com/colinleach/400B_Leach/blob/master/animations/collisions_disk.mp4

2.2. Mass profiles and rotation curves

Figure 6 shows the cumulative mass profile, by particle type and in total, for each galaxy. The center of each galaxy is dominated by baryonic matter with the DM halo becoming dominant at larger radii.

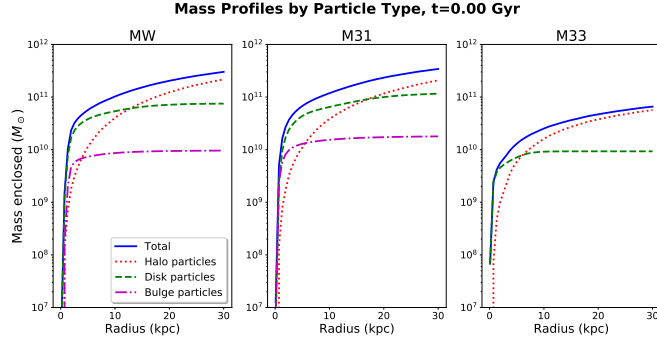


Figure 6. Mass profiles for each galaxy at the current epoch.

Figure 7 shows the rotation curves expected from these mass profiles. Without the DM halo the circular velocity would peak within a few kpc of the CoM then fall steadily at larger radii. With the more diffuse DM halo added, we see the relatively flat overall rotation curves which attracted the attention of 20th century astronomers including Zwicky (1933) and Rubin & Ford (1970)

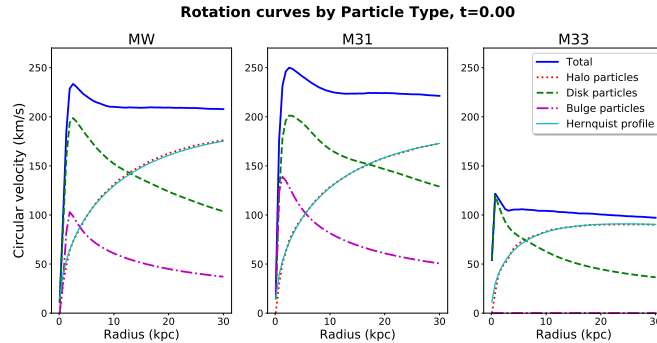


Figure 7. Rotation curves for each galaxy at the current epoch.

2.3. Stellar disk

2.3.1. Structure

TODO identify the bar?

TODO more on spiral arms

Disk structure and evolution may be easier to visualize if we transform to cylindrical coordinates (with the angular momentum vector along the z -axis) and use $r - \theta$ plots. Figure 8 shows this for the two large galaxies at several timepoints (as labelled). Spiral arms show up

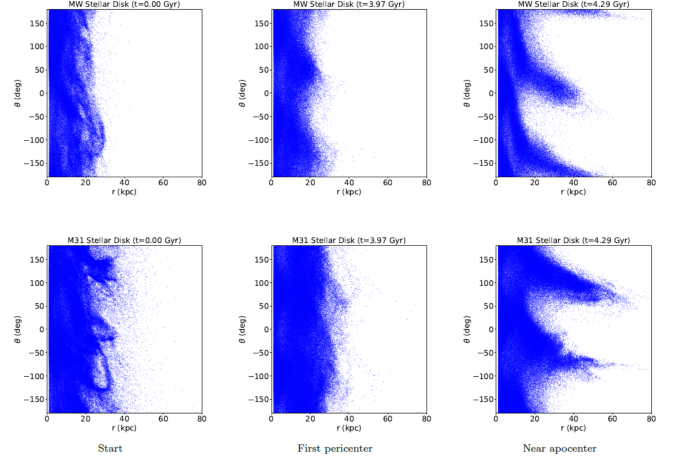


Figure 8. Disk particles from MW (top) and M31 (bottom) at three timepoints; cylindrical coordinates.

in both early in the simulation. First pericenter has, if little effect, but 0.3 Gyr later we see highly prominent tidal tails. These images are taken from a full animation for each galaxy, available online⁴

2.3.2. Inclinations

Galactic disks have a well-defined angular momentum vector which is relatively easy to calculate in this type of simulation. Figure 9 shows the angle each makes to the $X'-Y'$ plane over time.

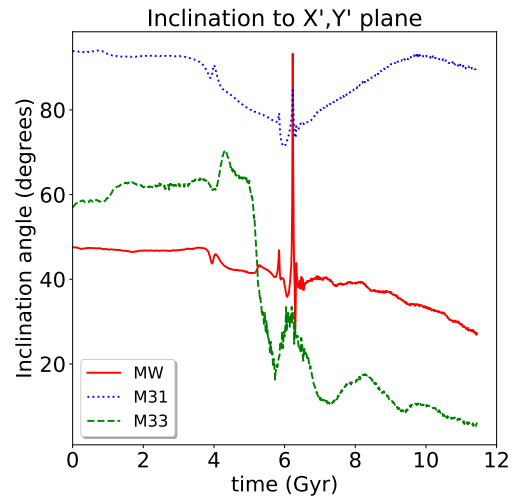


Figure 9. Angular momentum inclination angle to the X', Y' plane for each set of galactic disk particles.

⁴ https://github.com/colinleach/400B_Leach/tree/master/animations, files cyl_M*_disk.mp4

The mutual angle between galactic disks can have a significant impact on how tidal disruption and merger dynamics play out **TODO** ref?. This can be calculated from the vector dot products:

$$\theta = \arccos(\hat{L}_1 \cdot \hat{L}_2)$$

Results for the MW-M31 and M33-M31 pairs are shown in Figure 10. For MW-M31, the angle is largely stable until near first pericenter, when tidal forces bring the two disks closer to alignment. This trend continues slowly until near second pericenter. Surprisingly, the angle increases after merger, suggesting some partitioning of particles of different origin within the remnant.

TODO CHECK THIS AGAIN!

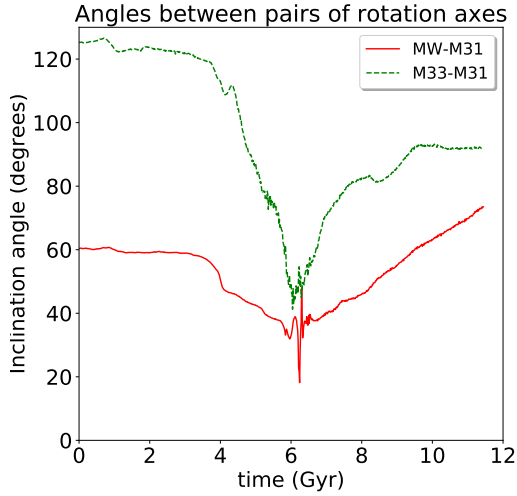


Figure 10. Angular momentum angles between pairs of galaxies.

The large variations in M33-M31 angles are indicative of the extensive tidal disruption of the much smaller M33 galaxy. Details are outside the scope of the present paper.

2.3.3. Velocity dispersion

The changes in velocity dispersion of disk particles originating from each galaxy are shown in Figure 11. The small periodic oscillation seen from the start, especially in M31, appears to be caused by deviations from radial symmetry in the disk: spiral arms and an increasingly prominent bar. Small MW spikes at initial pericenter (around 4 Gyr) and much larger ones at merger (around 6 Gyr) are clearly visible.

M33 is on an irregular, elliptical and decaying orbit about the MW-M31 merger remnant after about 6.5 Gyr. Velocity dispersion appears to peak at intervals.

This perhaps corresponds to successive pericenters when M33 experiences maximal tidal disruption, but this will need further analysis.

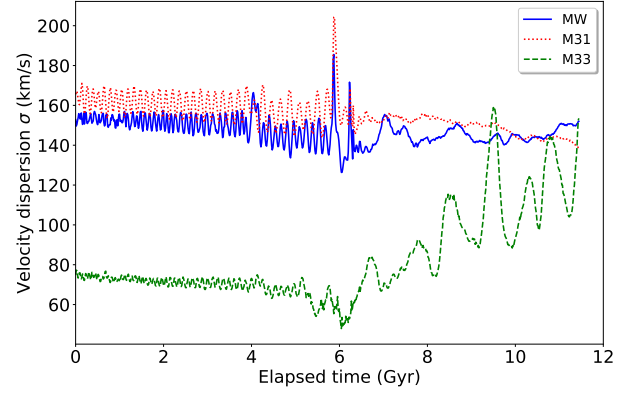


Figure 11. Velocity dispersion of disk particles from each galaxy over time.

TODO disk rotation curve, V_{rot}/σ

2.4. Stellar Bulge

A bulge is present in the MW and M31 but not M33. This region of generally older stars extends further above and below the central plane than disk stars. Kinematics of the bulge are more typical of an elliptical galaxy than a spiral disk.

In a study of elliptical galaxies, de Vaucouleurs showed that surface brightness falls off exponentially from the center and approximately as the one-fourth power of radius (de Vaucouleurs 1948). Later work found that this was too restrictive for a wider population of galaxies, so Sérsic generalized the formula to have the inverse exponential n as an additional free parameter (Sérsic 1963):

$$\log_{10} \left(\frac{I(r)}{I_e} \right) = -3.3307 \left[\left(\frac{r}{R_e} \right)^{1/n} - 1 \right]$$

Here R_e is the radius with which half the light is emitted, I_e is the surface brightness at R_e and n is the Sérsic parameter.

This formula is intended for analyzing photographic images and is in terms of light intensity. We have no brightness data in the current simulation, but for systems with few young blue stars we can assume the stellar mass to light ratio $M_*/L \sim 1$. This is probably a reasonable approximation for undisturbed bulges and for an elliptical merger remnant long after the collision. R_e is then the radius enclosing half the mass.

We can see from Figure 12 that for each galaxy the bulge half-mass radius is fairly stable up to the collision and merger of MW and M31. After a period of disturbance, they again become stable at a higher level. The

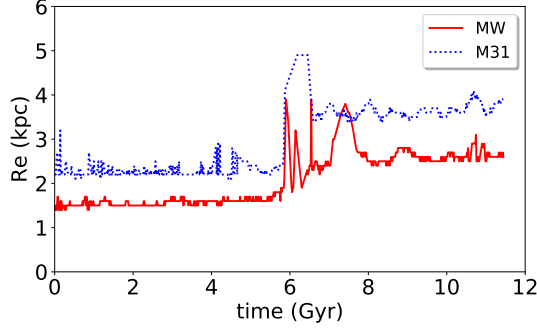


Figure 12. Half-mass radius for bulge particles.

M31 bulge is more diffuse than the MW bulge throughout, and the ex-bulge stars are clearly not randomized in the merger remnant: ex-M31 stars tend towards larger radii than ex-MW stars.

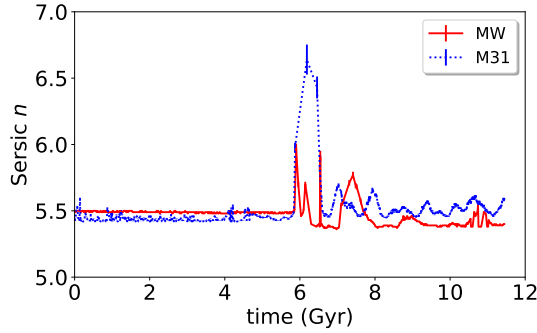


Figure 13. Sérsic n for bulge particles, with 1σ error bars.

The Sérsic parameter n was estimated by a nonlinear least squares fit to the bulge mass profile. As shown in Figure 13 it is fairly constant around 5.5 for any period with meaningful data. The spikes around 6 Gyr should probably be ignored: many values in this collision period are missing, as the least-squares fit failed, and the available data has substantially larger error bars than during stable epochs.

The larger half-mass radius of M31 is reflected in the mass density profile, as shown in Figure 14. MW bulge stars have a higher central peak, M31 bulge stars are more numerous at larger radii. This is true both early in the simulation, and in the merger remnant at late times. For both galaxy bulge stars, the central peak is less pronounced post-merger.

The Sérsic fit for both galaxy bulges looks reasonable outside the central density peak, as shown for the MW in Figure 15. The plot for M31 (not included here) is very similar.

2.5. Dark Matter halo

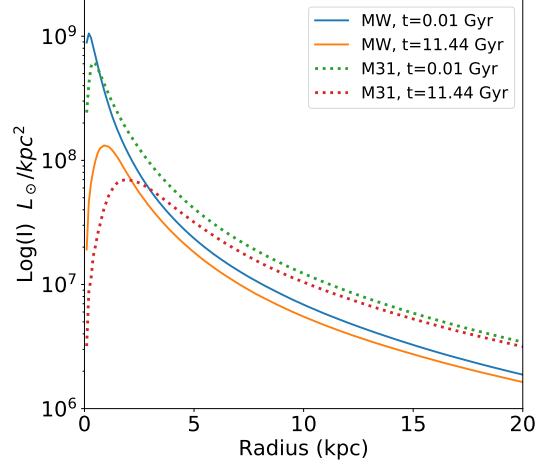


Figure 14. Bulge mass density profile for both galaxies at the beginning and end of the simulation.

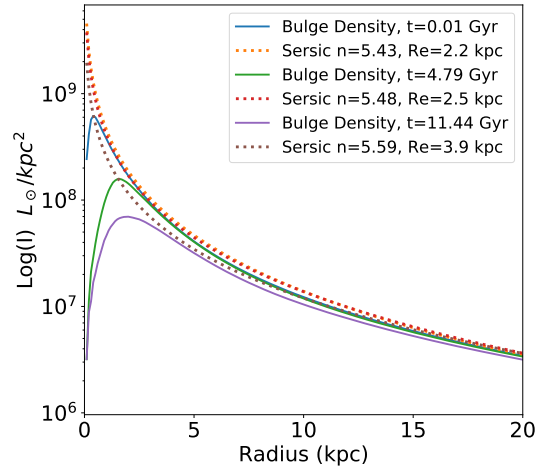


Figure 15. MW bulge mass density profiles and Sérsic best fits. Time points are the beginning, the pre-merger pericenter, and the end of the simulation

2.5.1. Halo mass profile

Figure 7 also adds a theoretical curve in which the DM halo is fitted by a Hernquist profile (Hernquist 1990). The cumulative mass out to radius r is given by

$$M(r) = M_h \frac{r^2}{(a + r)^2}$$

where M_h is the total mass of halo particles (see Table 2) and a is a scale radius which encloses a quarter of the halo mass. Non-linear least squares fitting, similar to that used for Sérsic profiles in a previous section, gave scale radii of 61.1 kpc for MW and M31, 24.3 kpc for M33 at $t = 0$.

Time evolution of the scale radius a is shown in Figure 16. The MW and M31 remain very similar through

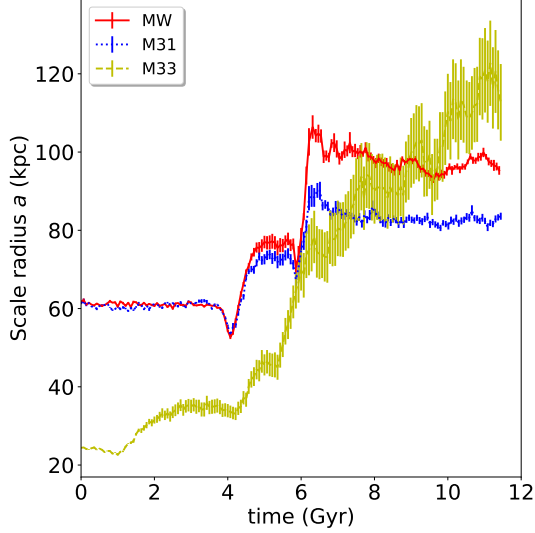


Figure 16. Hernquist scale radius a for DM halo particles originating from each galaxy, with 1σ error bars.

first pericenter, then start to diverge with MW particles tending to a larger radius than M31. This becomes most pronounced during and after merger. The dissimilar distribution in the merger remnant will be discussed in a later section.

The scale radius for M33 grows inexorably as the original halo is scattered by tidal forces. Figure 16 also shows the increasingly wide error bars for M33: halo particles for this galaxy are no longer well fitted by a Hernquist profile.

2.5.2. Halo rotation

The specific angular momentum \vec{h} can be calculated from

$$\vec{h} = \frac{\sum_i \vec{r}_i \times m_i \vec{v}_i}{\sum_i m_i}$$

The halo specific angular momentum for each large galaxy is shown in Figure 17. It appears that both are barely rotating at the current epoch, but spin up rapidly during first pericenter and again around the time of merger, as tidal forces convert orbit angular momentum into spin angular momentum. Differences in the remnant will be discussed in a later section.

Data for M33 is omitted from Figure 17 for clarity. The spin-up is much more dramatic for this minor galaxy, with peaks approaching $140 \text{ kpc}^2/\text{Myr}$, making it unsuitable to plot on the same axes.

2.6. MW-M31 Close approach

2.6.1. Inclinations

The MW and M31 disks have angular momentum vectors inclined at an angle of 52° to each other shortly before pericenter, making this a prograde approach.

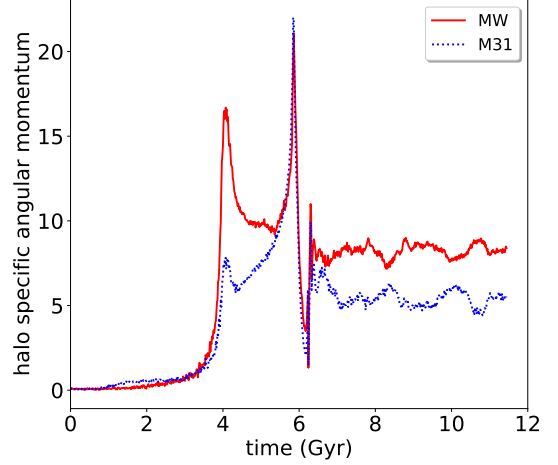


Figure 17. Specific angular momentum for halo particles of each galaxy about its CoM (kpc^2/Myr).

TODO Clarify this!

2.6.2. Tidal tails and bridges

The presence of long, symmetrical tails giving some galaxies a distinct ‘S’-shape has been described at least as far back as Zwicky (1955). Some astronomers postulated that these were the result of tidal forces during close, glancing encounters, but this was often contested until a detailed computational study by Toomre & Toomre (1972).

Reviewing a broad range of N-body simulations, Barnes & Hernquist (1992) noted that “such features are clearly *relics* of recent collisions rather than ongoing interactions.” In our simulation, both MW and M31 disks remain near-circular during much of the close approach, but conspicuous tails develop as the centers then move further apart: see Figure 8 and the animations referred to in Footnote 3. We also see a more sparsely-populated bridge forming between the galaxies.

To determine the nature and origin of stars in this region, a manual selection was performed as in Figure 18. Stars within the yellow rectangle (left panel) are shown with velocity vectors (center panel) and origin (right panel). Velocities are mostly moderate (mean 195 km/s , range $19\text{--}586 \text{ km/s}$), with relatively few stars having high kinetic energy.

It appears from the right panel that stars in the tail regions originate in the corresponding disk. The bridge region is more mixed and appears to have a high proportion of former bulge stars. To study this further the coordinate system was transformed to place the large galaxy CoMs on the x -axis at $\pm 64 \text{ kpc}$, as in Figure 19. It is clear in this view that one MW tail is oriented approximately towards the center of M31.

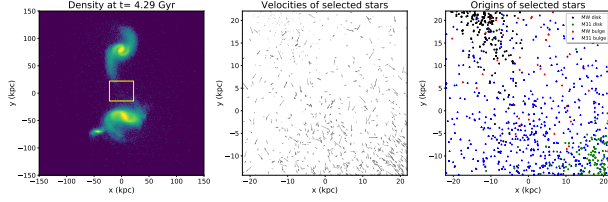


Figure 18. Manual selection of bridge particles at 0.33 Gyr after the first MW-M31 pericenter. The left panel shows stellar surface density and the selected region. The center panel shows velocity vectors for these stars and the right panel shows origin by galaxy and particle type. Orientation is with MW top, M31 bottom and M33 lower left.

TODO make this page-width in final layout

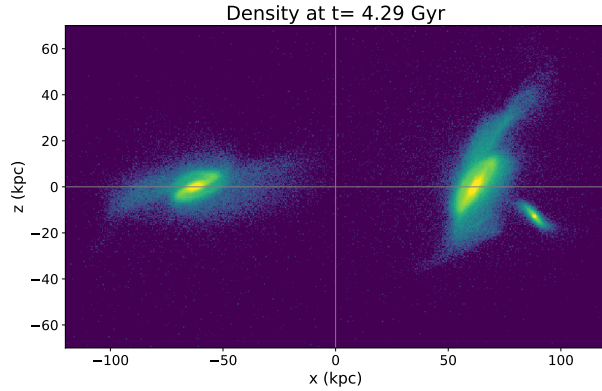


Figure 19. View along the midplane between the galactic centers, MW on the left.

Table 3. Particle counts close to the midplane

	Bulge	Disk	Total
MW	305	1317	1622
M31	1137	4	1141
Total	1442	1321	2763

The different orientations mean that symmetry about the midplane is imperfect, so the “bridge” region was taken as $-20 < x < 30$ kpc. A count of stars in this region is shown in Table 3. This confirms that the largest populations are MW disk stars (mostly in a relatively dense tail) and M31 bulge stars (more widely dispersed).

TODO identify, trace history, trace fate

TODO Jacobi radius

TODO Tail kinematics: σ , energy

TODO Lifetime of tails

2.6.3. Mass transfer

Stars are scattered from galaxies even in normal times, and this can be expected to increase significantly during near-misses and collisions. To get a first impression of how many stars and DM particles may end up closer to a different galaxy, we looked at the relative distances of each particle to each of the three galaxy CoMs. It should be emphasized that kinematics is not considered at this stage, so nothing can be said about which particles are gravitationally bound.

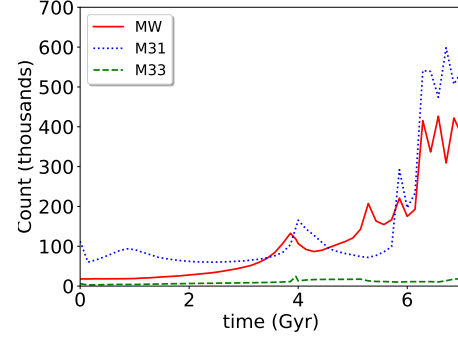


Figure 20. Particles closer to a different CoM.

Figure 20 shows that some particles are far from their notional galaxy even at the start. This increases somewhat during first pericenter around 4 Gyr, then jumps permanently during the second pericenter and merger. The plot cuts off at 7 Gyr because it becomes meaningless to consider the MW/M31 CoMs as separate points post-merger.

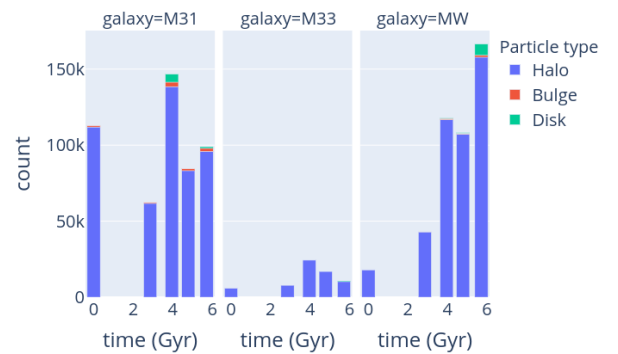


Figure 21. Particles closer to a different CoM.

Figure 21 looks at a few timepoints by particle type, showing that the overwhelming majority of these particles are from the DM halo. This is unremarkable, given the prevalence of these particles at large radii and their correspondingly weak gravitational binding.

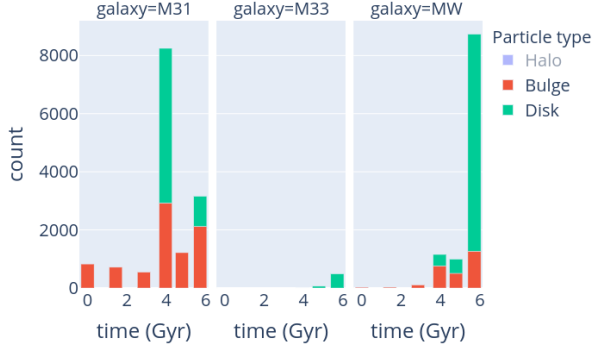


Figure 22. Luminous particles closer to a different CoM (DM halo hidden).

To focus on the baryonic matter, Figure 22 hides the DM halo and expands the y -axis to show only bulge and disk particles. There are significant numbers of M31 bulge particles at all timepoints, mostly reflecting the proximity of M33. The last three bars on each panel correspond to first pericenter, apocenter, and second pericenter. M31 disk particle numbers jump at first pericenter but these apparently remain bound to the original galaxy: virtually all return to M31 before apocenter.

2.7. MW-M31 merger

After second pericenter, the MW and M31 never fully separate and eventually merge. Their mass ratio is 1:1.6 for stellar matter and 1:1 when the DM halo is included. This is thus a ‘major merger’, which is generally taken to mean closer than 1:4 luminosity ratio (or mass ratio as a proxy). A 1:1 mass ratio has been reported (Boylan-Kolchin et al. 2008; Ji et al. 2014) to lead to the shortest coalescence time.

The 3D trajectories are complex, but Figures 23 and 24 are snapshots which attempts to show this. The MW CoM is always at the origin and the points show the M31 CoM at regular 14.3 Myr intervals. First pericenter is at upper left (outer), apocenter at the bottom, second pericenter in the tight reversal at upper left. The path is smooth up to 6.1 Gyr then becomes more chaotic.

TODO changes in mass profile

2.7.1. Inclinations

TODO Relative rotation axes of disks – prograde?

2.8. MW-M31 merger remnant

2.8.1. Remnant shape

TODO boxiness?

We can expect the remnant to settle over time into a triaxial ellipsoid **TODO** ref?. In observational astronomy it would be usual to determine the shape by fitting

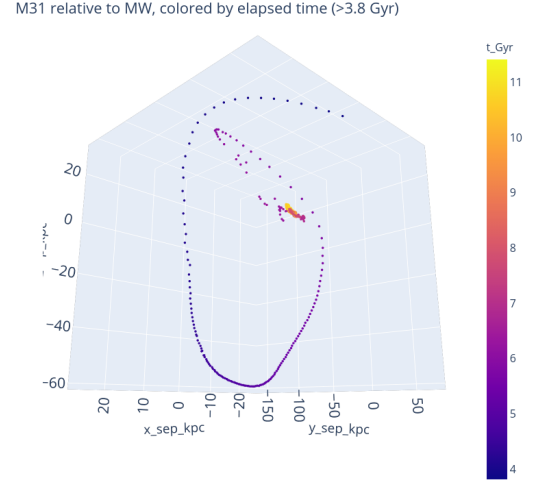


Figure 23. Approach and merger in a MW-centric coordinate frame. Points are spaced at 14.3 Myr intervals.).

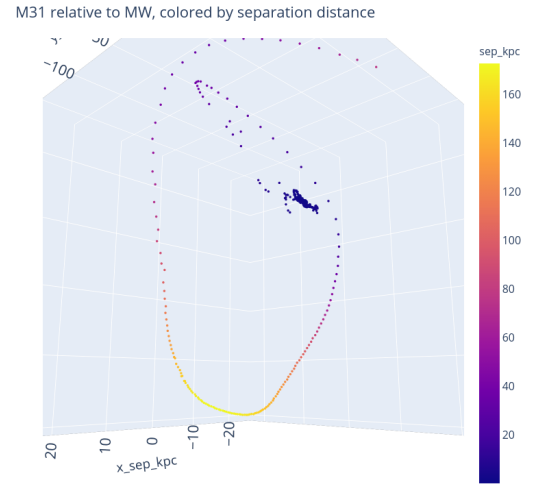


Figure 24. Approach and merger. Similar to Figure 23 except the color coding is by separation.

ellipses to surface brightness contours. That is also possible for the simulation, but for a highly-determined system for which we know the mass and position of every particle there are other options.

If we combine all the baryonic matter (disk and bulge) from both MW and M31, there are 1.12×10^6 particles to consider. Some of these have been ejected to large radius where they have an exaggerated effect on the moment of inertia, so only those within 40 kpc of the CoM were used in the calculation.

In the original coordinates, the moment of inertia tensor is symmetrical ($I_{ij} = I_{ji}$), 3×3 :

$$I = \begin{bmatrix} I_{xx} & I_{xy} & I_{xz} \\ I_{yx} & I_{yy} & I_{yz} \\ I_{zx} & I_{zy} & I_{zz} \end{bmatrix}$$

$$I_{total} \approx \begin{bmatrix} 2.44 \times 10^4 & 2.55 \times 10^2 & 1.43 \times 10^3 \\ 2.55 \times 10^2 & 1.91 \times 10^4 & -1.71 \times 10^1 \\ 1.43 \times 10^3 & -1.71 \times 10^1 & 2.22 \times 10^4 \end{bmatrix}$$

The orientation is arbitrary at this stage. To get principal axes we need the eigenvalues and eigenvectors of I .

The eigenvalues give the moments of inertia about the principal axes, in arbitrary units scaled such that $A = 1$:

$$A = 1.0, \quad B = 0.95, \quad C = 0.78$$

The eigenvectors give an orthonormal coordinate system oriented along the principal axes:

$$\begin{aligned} \hat{v}_a &= \langle -0.114, -0.416, +0.902 \rangle \\ \hat{v}_b &= \langle -0.524, +0.797, +0.302 \rangle \\ \hat{v}_c &= \langle -0.844, -0.438, -0.309 \rangle \end{aligned}$$

The moment of inertia of an ellipsoid with semi-major axes a, b, c is $A = k(b^2 + c^2)$ where k is a constant that depends on total mass. Other axes have the same form by symmetry. Solving for a, b, c and normalizing gives:

$$a = 1.0, \quad b = 0.94, \quad c = 0.77$$

So the remnant is triaxial (low-symmetry, with $a \neq b \neq c$). However, the minor axis c is significantly smaller than the other two: the ellipsoid is approximately prolate ($a \approx b > c$).

This was repeated for each subgroup by particle origin. The numbers involved are shown in Table 3.

Table 3. Counts of particles by origin (thousands)

Galaxy	Bulge	Disk	All
M31	95	600	695
MW	50	375	425
All	145	975	1120

The relative axis lengths are shown in Table 4. All subgroups are triaxial (low-symmetry, with $a \neq b \neq c$),

Table 4. Relative size of axes by particle origin

Galaxy	a	b	c
total	1.0	0.95	0.78
MW disk	1.0	0.95	0.64
MW bulge	1.0	0.96	0.71
M31 disk	1.0	0.91	0.82
M31 bulge	1.0	0.95	0.83

but ex-MW disk particles are distinctive in retaining a particularly flattened distribution.

The mutual inclination angles of the major axes are shown in Table 5. Again, the former disk particles are seen to retain a distinctive structure. Clearly this collision and a single merger is not sufficient to randomize stars within the remnant **TODO** refs?. Also, this is consistent with the understanding that relaxation times are very long in collisionless systems on the scale of elliptical galaxies (Binney & Tremaine 2008, Section 1.2)

Table 5. Mutual inclination angles of major axis by particle origin (degrees). Suffix indicates source: **disk**/**bulge**.

	Total	MWd	MWb	M31d	M31b
total	–	39.9	26.5	13.7	21.6
MWd	39.9	–	15.7	50.7	19.9
MWb	26.5	15.7	–	39.2	4.9
M31d	13.7	50.7	39.2	–	34.4
M31b	21.6	19.9	4.9	34.4	–

TODO Overlay this on contour fit to check it
TODO redo this for various radii cutoffs

2.8.2. Remnant mass distribution

The mass profile for each type of particle and overall is shown in Figure 25. This is similar to Figure 6, except that the radius now extends out to 100 kpc.

Previous sections have shown that MW and M31 particles remain somewhat distinct after merger. Figure 26 compares their mass profiles. For baryonic particles, ex-M31 masses are higher than ex-MW at most radii, reflecting the higher baryonic mass fraction in M31. The opposite effect might be expected for the DM halo, whose total mass was significantly higher in the MW (Table 2), but this is not seen out to 100 kpc. Fig-

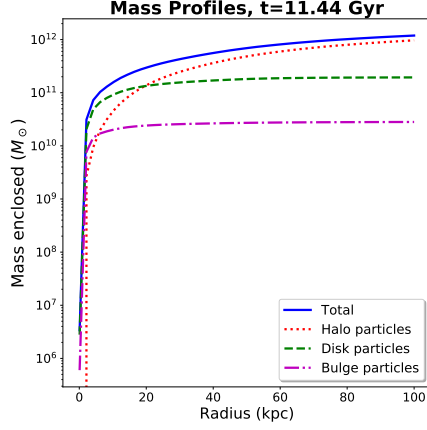


Figure 25. Mass profiles of the remnant by particle type.

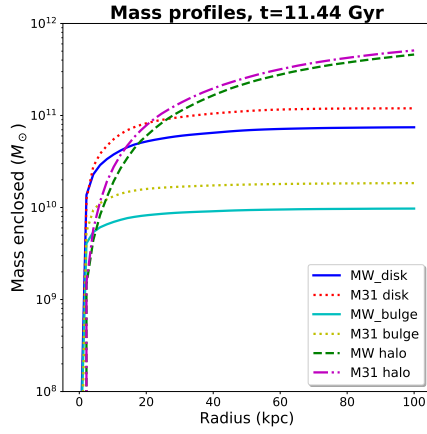


Figure 26. Mass profiles of the remnant by origin.

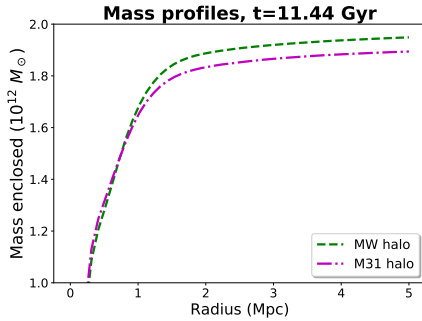


Figure 27. Mass profiles of the outer part of the remnant halo.

ure 27 suggests we have to go almost 1 Mpc out before MW particles become the largest halo component.

TODO Would be better to plot $\rho(r)$

TODO Does stellar density profile agree with predictions for elliptical galaxies?

Figure 30 shows Sérsic fits to the surface brightness profile (assuming $M_*/L \sim 1$).

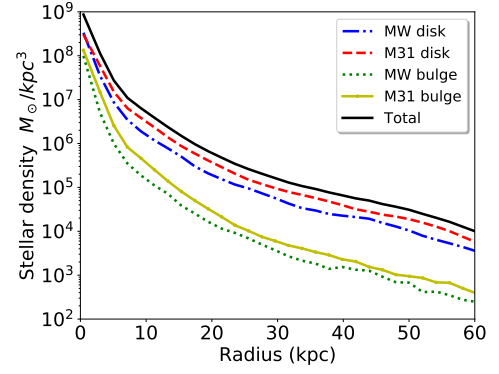


Figure 28. Spherically-averaged density profiles of the remnant luminous matter by origin.

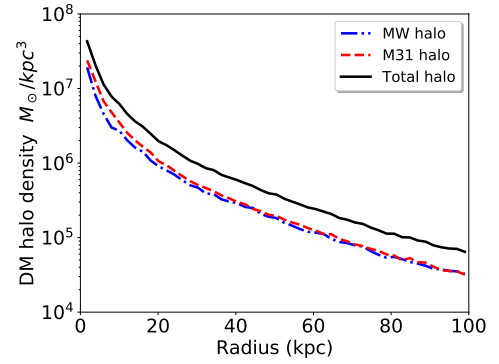


Figure 29. Spherically-averaged density profiles of the remnant halo by origin. Note the expanded x -axis relative to Figure 28

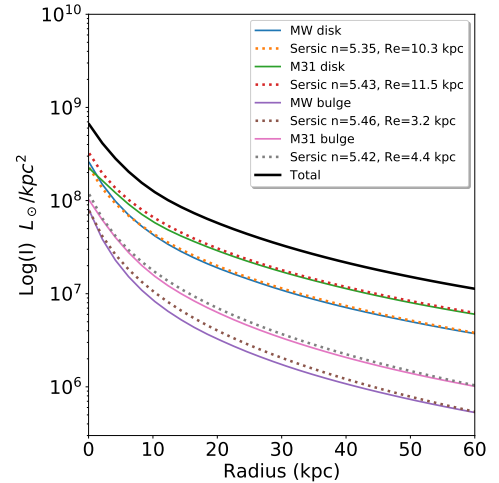


Figure 30. Surface brightness profiles of the remnant by origin.

The mass profile of DM particles in the remnant halo is well fit by a Hernquist profile, but there are some differences depending on origin as shown in Table 6

Table 6. Best-fit Hernquist a for remnant halo

Origin	$a \pm \text{StdDev (kpc)}$
total	84.5 ± 0.5
ex-MW	95.2 ± 1.4
ex-M31	82.3 ± 0.9

For comparison, the a values at $t = 0$ were

$$\text{MW} = 61.6 \pm 0.5 \text{ kpc}$$

$$\text{M31} = 61.4 \pm 0.2 \text{ kpc}$$

The overall time-dependence of Hernquist radii was shown in Figure 16.

2.8.3. Virial radius

The DM halo obviously has no sharp outer edge, it just gradually fades into the inter-galactic medium (IGM). One popular convention is to use the r_{200} or “virial radius” as a limit: the radius at which the density is $200\times$ the cosmological critical density ρ_c .

For a flat LambdaCDM cosmology, we can calculate the critical density from

$$\rho_c(t) = \frac{3H^2(t)}{8\pi G}$$

Currently (PlanckCollaboration et al. 2016) we have⁵

$$H(0) \equiv H_0 = 67.74 \text{ km/s/Mpc}$$

$$\rho_{c,0} = 127.35 \text{ } M_\odot/\text{kpc}^3$$

The simulation ends more than 11 Gyr in the future, so we need a different value for $H(t)$. By then the universe will be well into a Dark Energy-dominated epoch with near-exponential expansion. Then $\dot{H}(t) \approx 0$ and $H(t)$ asymptotically approaches its final value of $H_\infty \approx 57 \text{ km/s/Mpc}$.

This gives us a value of $\rho_{c,\infty} \approx 90 \text{ } M_\odot/\text{kpc}^3$. Then r_{200} is the radius at which the spherically-averaged remnant halo density falls below $1.8 \times 10^4 \text{ } M_\odot/\text{kpc}^3$. At the final timepoint, this is

$$r_{200} \approx 168 \text{ kpc}$$

The virial mass, enclosed within the virial radius, is $1.7 \times 10^{12} \text{ } M_\odot$, of which 87% is Dark Matter.

For comparison, if we used the current value $\rho_{c,0}$ throughout, the virial radius at the final timepoint

would be about 142 kpc and the virial mass falls to about $1.5 \times 10^{12} \text{ } M_\odot$.

TODO Some discussion would be useful!

2.8.4. Remnant angular momentum

The specific angular momentum \vec{h} was calculated for all the particles in the merger remnant and various subsets, as shown in Table 7. Differences tend to be small for stellar particles regardless of origin, larger for the ex-M31 halo and much larger for the ex-MW halo.

We showed in Figure 17 that halo angular momentum mostly arises from tidal forces during close approach and merger, and in Figure 16 that MW halo particles subsequently have a significantly larger scale radius than M31 halo particles. As specific angular momentum is a product of radius and tangential velocity, it seems reasonable that we see a higher value for ex-MW Dark Matter when it tends to be at larger radius.

Table 7. Specific angular momentum components for the merger remnant at $t=11.44$ Gyr ($\text{kpc}^2 / \text{Myr}$)

	\hat{h}_x	\hat{h}_y	\hat{h}_z	$ h $
total	0.64	0.03	-0.77	12.77
MW disk	0.65	-0.13	-0.75	6.43
M31 disk	0.53	-0.21	-0.82	6.28
MW bulge	0.62	-0.05	-0.78	6.80
M31 bulge	0.61	-0.12	-0.78	6.22
MW halo	0.66	0.09	-0.74	16.89
M31 halo	0.60	-0.08	-0.80	9.42

A previous section showed that the remnant is elliptical and particles of different orientation are oriented very differently (Table 5). When this analysis is repeated for the angular momentum vectors the mutual inclination angles are non-zero but generally quite small, as shown in Table 8.

For the aggregate of all DM particles in the remnant at this time, the angular momentum vector has orientation $\hat{h} = \langle 0.64, 0.03, -0.76 \rangle$, almost identical to the total for all particles (baryonic + DM) in the remnant. The magnitude $|h| = 13.15 \text{ kpc}^2/\text{Myr}$ is more than two orders of magnitude higher than the values for the individual galaxies about their respective CoM at the current epoch.

We showed in Figure 17 that halo angular momentum mostly arises from tidal forces during close approach and merger, and in Figure 16 that MW halo particles subsequently have a significantly larger scale radius than M31

⁵ Wendy Freedman might disagree (very eloquently), but let’s go with these values for now.

Table 8. Mutual inclination angles for rotation vectors in the merger remnant at $t=11.44$ Gyr (degrees)

	total	MWd	M31d	MWb	M31b	MWh	M31h
total	–	9.0	15.5	4.5	8.9	4.2	6.9
MWd	9.0	–	9.2	5.4	3.2	12.7	4.9
M31d	15.5	9.2	–	11.0	7.0	19.7	8.7
MWb	4.5	5.4	11.0	–	4.5	8.7	2.4
M31d	8.9	3.2	7.0	4.5	–	13.1	2.7
MWh	4.2	12.7	19.7	8.7	13.1	–	11.1
M31h	6.9	4.9	8.7	2.4	2.7	11.1	–

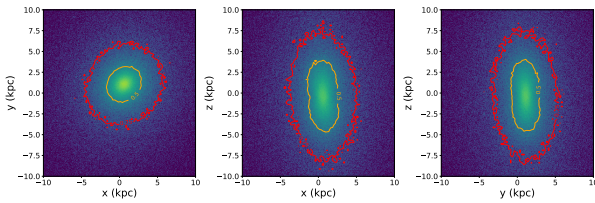
halo particles. As specific angular momentum is a product of radius and tangential velocity, it seems reasonable that we see a higher value for ex-MW Dark Matter when it tends to be at larger radius.

2.8.5. Remnant stellar kinematics

It was shown in (Cox et al. 2006) that simulated mergers lead to substantially different rotational kinematics if the galaxies are gas-poor (“dry”) and the collision is dissipationless versus gas-rich, dissipational collisions.

Initially, the stellar particles (from all origins) were used to calculate an angular momentum vector \hat{L} , then the coordinate system was rotated to place this along the z -axis. We might have expected the principal axes of the ellipsoid to correspond in some simple way to this projection, but this was found to be far from the case.

More intuitive results were obtained once the \hat{L} calculation was limited to stars within a limited radius of the CoM. Figure 31 uses a 50 kpc limit and shows that the major axis is approximately parallel to the rotation axis. Centering is clearly not perfect **TODO** can this be improved?

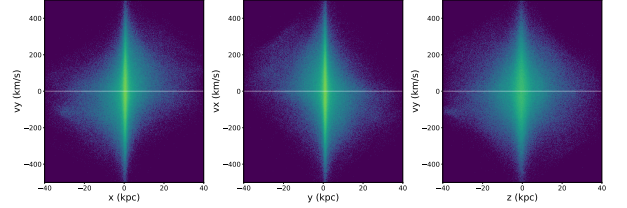
**Figure 31.** Luminous star density of the MW-M31 remnant in three orthogonal projections. Left panel looks down the \hat{L} axis, mid/right panels have this vertical.

TODO Is it a fast or slow rotator?

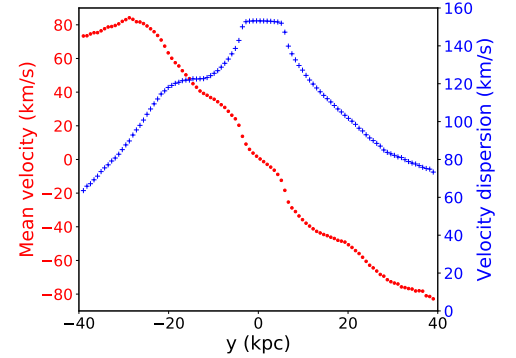
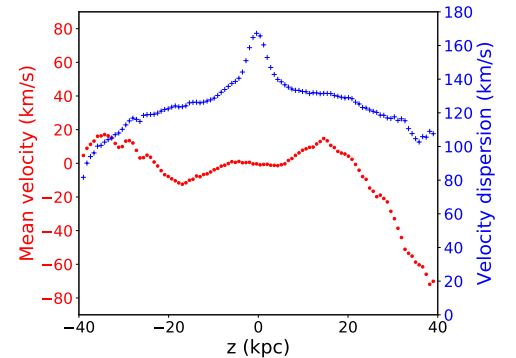
TODO Does the virial theorem work to return the total baryonic mass?

Figure 32 shows phase diagrams in various orientations. There is a fairly clear velocity asymmetry along

the x - and y -axes, perpendicular to \hat{L} , but not along the z -axis.

**Figure 32.** Phase diagrams of the MW-M31 remnant, orthogonal views.

Mean radial velocities \bar{v} and velocity dispersions σ were calculated by binning along the y -axis (Figure 33) and the z -axis (Figure 34). The results are not entirely simple and regular, but the former shows clear rotation with $v_{\max} \approx 83$ km/s. As expected, the latter has smaller and more random velocities with a somewhat higher dispersion.

**Figure 33.** Velocity (red circles) and dispersion (blue +) by radius, y -axis: perpendicular to the angular momentum vector.**Figure 34.** Velocity and dispersion by radius, z -axis: along the angular momentum vector.

Central velocity dispersion is about 153 km/s, so the ratio v_{\max}/σ is 0.54.

For oblate isotropic rotators with ellipticity ϵ , there is a relation **TODO** Binney78 ref

$$(V/\sigma) = \sqrt{\epsilon/(1-\epsilon)}$$

For the stellar remnant we have $\epsilon \approx 0.5$, so $(V/\sigma) \approx 1$.

2.8.6. Remnant halo kinematics

The literature consensus is that halo shapes are supported by anisotropic velocity dispersions, not spin (Frenk & White 2012). They can acquire angular momentum through tidal torques, as we already saw for each galaxy in Figure 17. This is often characterized by a dimensionless spin parameter:

$$\lambda = \frac{J|E|^{1/2}}{GM^{5/2}}$$

where J is the magnitude of the angular momentum vector, E is the total energy and M is the halo mass. Often, these are taken as the values inside the virial radius, ignoring DM particles lost to the IGM.

Total energy E is the sum of kinetic energy K and potential energy W . We have the mass and velocity of every particle so

$$K = \sum_i \frac{1}{2} m_i v_i^2$$

Potential energy is more challenging to calculate. In general (Binney & Tremaine 2008, section 2.1):

$$W = \frac{1}{2} \int d^3 \mathbf{x} \rho(\mathbf{x}) \Phi(\mathbf{x})$$

We would need this to calculate the highly-disrupted situation shortly after collision and merger (Binney & Tremaine 2008, section 8.2). For simplicity, we concentrate here on the final timepoint about 5 Gyr after merger, and assume that the remnant halo is by then close to virial equilibrium. Then $E \approx -K$ and the calculation is very much easier.

Other than potential energy, relevant values for the remnant halo vary little over time. Figure 35 shows that angular momentum, kinetic energy and virial mass remain within $\pm 20\%$ of their final value.

The final timepoint of the simulation gives these results:

$$J = 2.9 \times 10^{12} M_{\odot} \text{ kpc}^2 / \text{Myr}$$

$$K = 1.5 \times 10^{65} \text{ erg}$$

$$M = 1.3 \times 10^{12} M_{\odot}$$

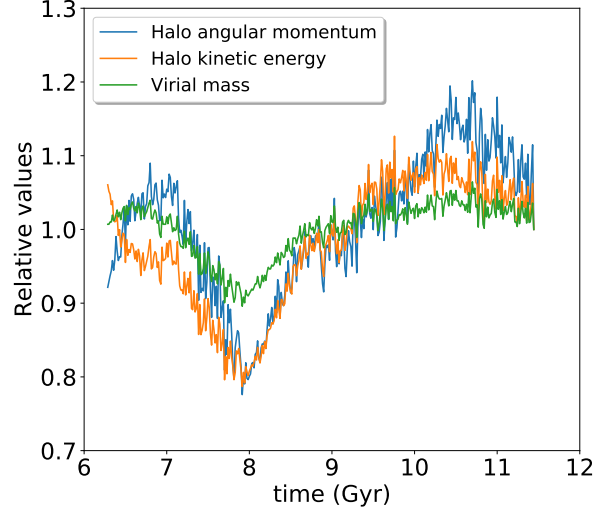


Figure 35. Relative values for the remnant halo over time; final timepoint = 1.

Unfortunately, this gives a spin parameter $\lambda \approx 30$, about 2 orders of magnitude higher than expected.

TODO Figure out what went wrong!

TODO remnant DM σ

TODO $V_{\text{esc}}(r)$

3. DISCUSSION AND CONCLUSIONS

TODO add some!

4. ACKNOWLEDGMENTS

The author is grateful to Professor Gurtina Besla for teaching the class on which this paper is based and for allowing this rather geriatric student to participate, as well as providing all the raw data from the earlier simulation described in vdM12. Also to Rixin Li for valuable coding advice.

This work relied on a range of open-source software packages, many of them sponsored by NumFOCUS⁶ for the benefit of us all:

- NumPy (van der Walt et al. 2011)
- Matplotlib (Hunter 2007)
- pandas (McKinney 2010)
- Astropy (Astropy Collaboration et al. 2013)
- SciPy (Virtanen et al. 2020)
- IPython (Perez & Granger 2007)
- Jupyter (Kluyver et al. 2016)
- conda-forge⁷

⁶ <https://numfocus.org/>

⁷ <https://conda-forge.org/>

Additionally, `mpl-scatter-density`⁸ and `Plotly`⁹ were used in preparing the figures.

REFERENCES

- Astropy Collaboration, Robitaille, T. P., Tollerud, E. J., et al. 2013, *A&A*, 558, A33, doi: [10.1051/0004-6361/201322068](https://doi.org/10.1051/0004-6361/201322068)
- Barnes, J. E., & Hernquist, L. 1992, *Annual Review of Astronomy and Astrophysics*, 30, 705, doi: [10.1146/annurev.aa.30.090192.003421](https://doi.org/10.1146/annurev.aa.30.090192.003421)
- Binney, J., & Tremaine, S. 2008, *Galactic Dynamics: Second Edition*, by James Binney and Scott Tremaine. ISBN 978-0-691-13026-2 (HB). Published by Princeton University Press, Princeton, NJ USA, 2008. <http://adsabs.harvard.edu/abs/2008gady.book.....B>
- Bodenheimer, P., Laughlin, G. P., Różycka, M., & Yorke, H. W. 2007, *Numerical Methods in Astrophysics: An Introduction* (CRC Press). <http://adsabs.harvard.edu/abs/2007nmai.conf....B>
- Boylan-Kolchin, M., Ma, C.-P., & Quataert, E. 2008, *Monthly Notices of the Royal Astronomical Society*, 383, 93, doi: [10.1111/j.1365-2966.2007.12530.x](https://doi.org/10.1111/j.1365-2966.2007.12530.x)
- Brown, A. G. A., Vallenari, A., Prusti, T., et al. 2018, *Astronomy & Astrophysics*, 616, A1, doi: [10.1051/0004-6361/201833051](https://doi.org/10.1051/0004-6361/201833051)
- Cox, T. J., Dutta, S. N., Di Matteo, T., et al. 2006, *The Astrophysical Journal*, 650, 791, doi: [10.1086/507474](https://doi.org/10.1086/507474)
- de Vaucouleurs, G. 1948, *Annales d’Astrophysique*, 11, 247. <http://adsabs.harvard.edu/abs/1948AnAp...11..247D>
- Frenk, C. S., & White, S. D. M. 2012, *Annalen der Physik*, 524, 507, doi: [10.1002/andp.201200212](https://doi.org/10.1002/andp.201200212)
- Hernquist, L. 1990, *The Astrophysical Journal*, 356, 359, doi: [10.1086/168845](https://doi.org/10.1086/168845)
- Hunter, J. D. 2007, *Computing in Science & Engineering*, 9, 90, doi: [10.1109/MCSE.2007.55](https://doi.org/10.1109/MCSE.2007.55)
- Ji, I., Peirani, S., & Yi, S. K. 2014, *Astronomy & Astrophysics*, 566, A97, doi: [10.1051/0004-6361/201423530](https://doi.org/10.1051/0004-6361/201423530)
- Kluyver, T., Ragan-Kelley, B., Pérez, F., et al. 2016, in *Positioning and Power in Academic Publishing: Players, Agents and Agendas*, ed. F. Loizides & B. Schmidt, IOS Press, 87 – 90
- Marel, R. P. v. d., Besla, G., Cox, T. J., Sohn, S. T., & Anderson, J. 2012a, *The Astrophysical Journal*, 753, 9, doi: [10.1088/0004-637X/753/1/9](https://doi.org/10.1088/0004-637X/753/1/9)
- Marel, R. P. v. d., Fardal, M., Besla, G., et al. 2012b, *The Astrophysical Journal*, 753, 8, doi: [10.1088/0004-637X/753/1/8](https://doi.org/10.1088/0004-637X/753/1/8)
- Marel, R. P. v. d., Fardal, M. A., Sohn, S. T., et al. 2019, *The Astrophysical Journal*, 872, 24, doi: [10.3847/1538-4357/ab001b](https://doi.org/10.3847/1538-4357/ab001b)
- McKinney, W. 2010, in *Proceedings of the 9th Python in Science Conference*, ed. Stéfan van der Walt & Jarrod Millman, 56 – 61, doi: [10.25080/Majora-92bf1922-00a](https://doi.org/10.25080/Majora-92bf1922-00a)
- Mo, H., van den Bosch, F. C., & White, S. 2010, *Galaxy Formation and Evolution*, by Houjun Mo, Frank van den Bosch, Simon White, Cambridge, UK: Cambridge University Press, 2010. <http://adsabs.harvard.edu/abs/2010gfe..book.....M>
- Perez, F., & Granger, B. E. 2007, *Computing in Science & Engineering*, 9, 21, doi: [10.1109/MCSE.2007.53](https://doi.org/10.1109/MCSE.2007.53)
- PlanckCollaboration, Ade, P. A. R., Aghanim, N., et al. 2016, *Astronomy & Astrophysics*, 594, A13, doi: [10.1051/0004-6361/201525830](https://doi.org/10.1051/0004-6361/201525830)
- Rubin, V. C., & Ford, Jr., W. K. 1970, *The Astrophysical Journal*, 159, 379, doi: [10.1086/150317](https://doi.org/10.1086/150317)
- Sérsic, J. L. 1963, *Boletín de la Asociación Argentina de Astronomía La Plata Argentina*, 6, 41. <http://adsabs.harvard.edu/abs/1963BAAA....6...41S>
- Toomre, A., & Toomre, J. 1972, *The Astrophysical Journal*, 178, 623, doi: [10.1086/151823](https://doi.org/10.1086/151823)
- van der Walt, S., Colbert, S. C., & Varoquaux, G. 2011, *Computing in Science & Engineering*, 13, 22, doi: [10.1109/MCSE.2011.37](https://doi.org/10.1109/MCSE.2011.37)
- Virtanen, P., Gommers, R., Oliphant, T. E., et al. 2020, *Nature Methods*, doi: <https://doi.org/10.1038/s41592-019-0686-2>
- Zwicky, F. 1933, *Helvetica Physica Acta*, 6, 110. <http://adsabs.harvard.edu/abs/1933AcHPh...6..110Z>
- . 1955, *Publications of the Astronomical Society of the Pacific*, 67, 232, doi: [10.1086/126807](https://doi.org/10.1086/126807)

⁸ <https://github.com/astrofrog/mpl-scatter-density>

⁹ <https://plotly.com/python/>